



ISTITUTO NAZIONALE DI RICERCA METROLOGICA Repository Istituzionale

Dewetting Process in Ni-Mn-Ga Shape-Memory Heusler: Effects on Morphology, Stoichiometry and Magnetic Properties

Original

Dewetting Process in Ni-Mn-Ga Shape-Memory Heusler: Effects on Morphology, Stoichiometry and Magnetic Properties / Ghahfarokhi, Mt; Celegato, F; Barrera, G; Casoli, F; Tiberto, P; Albertini, F. - In: CRYSTALS. - ISSN 2073-4352. - 12:12(2022), p. 1826. [10.3390/cryst12121826]

Availability:

This version is available at: 11696/75946 since: 2023-02-21T13:18:35Z

Publisher:

MDPI

Published

DOI:10.3390/cryst12121826

Terms of use:





This article is made available under terms and conditions as specified in the corresponding bibliographic description in the repository

Publisher copyright

(Article begins on next page)

Article

Dewetting Process in Ni-Mn-Ga Shape-Memory Heusler: Effects on Morphology, Stoichiometry and Magnetic Properties

Milad Takhsha Ghahfarokhi ^{1,*}, Federica Celegato ², Gabriele Barrera ², Francesca Casoli ^{1,*}, Paola Tiberto ² and Franca Albertini ¹

¹ Institute of Materials for Electronics and Magnetism, National Research Council (IMEM-CNR), Parco Area delle Scienze 37/A, 43124 Parma, Italy

² Advanced Materials Metrology and Life Sciences (INRiM), Strada delle Cacce 91, 10135 Turin, Italy

* Correspondence: milad.takhsha@imem.cnr.it (M.T.G.); francesca.casoli@imem.cnr.it (F.C.)

Abstract: In this work, dewetting process has been investigated in shape-memory Heuslers. To this aim, series of high-temperature annealing (1100–1150 K) have been performed at high vacuum (time is varied in the range of 55–165 min) in Ni-Mn-Ga epitaxial thin films grown on MgO(001). The process kinetics have been followed by studying the evolution of morphology and composition. In particular, we report the initiation of the dewetting process by the formation of symmetric holes in the films. The holes propagate and integrate, leaving micrometric and submicron islands of the material, increasing the average roughness of the films by a factor of up to around 30. The dewetting process is accompanied by severe Ga and Mn sublimation, and Ni-Ga segregation, which significantly modify the magnetic properties of the films measured at each stage. The annealed samples show a relatively weak magnetic signal at room temperature with respect to the pristine sample.



Citation: Takhsha Ghahfarokhi, M.; Celegato, F.; Barrera, G.; Casoli, F.; Tiberto, P.; Albertini, F. Dewetting Process in Ni-Mn-Ga Shape-Memory Heusler: Effects on Morphology, Stoichiometry and Magnetic Properties. *Crystals* **2022**, *12*, 1826. <https://doi.org/10.3390/cryst12121826>

Academic Editor: Jacek Ćwik

Received: 8 November 2022

Accepted: 12 December 2022

Published: 15 December 2022

Publisher's Note: MDPI stays neutral with regard to jurisdictional claims in published maps and institutional affiliations.



Copyright: © 2022 by the authors. Licensee MDPI, Basel, Switzerland. This article is an open access article distributed under the terms and conditions of the Creative Commons Attribution (CC BY) license (<https://creativecommons.org/licenses/by/4.0/>).

Keywords: magnetic shape memory alloys; multifunctional Heusler compounds; solid-state dewetting; annealing; morphology; stoichiometry; magnetic properties

1. Introduction

Small-scale magnetic-shape-memory (MSM) Heuslers are promising for a vast variety of applications in automotive, aerospace, biology and robotics, serving as smart moving components, sensors, and energy harvesters [1–3], as well as being the active materials in multicaloric cooling systems [4,5]. The material down-scaling is specifically important, as it can improve the integration capability into small-scale devices [2,5,6]. It can also enhance the mechanical properties and enable manufacturing complex shapes, giving rise to the idea of “crushing down the material and building back better”. For instance, there have recently been a few pioneering works reporting the use of MSM Heusler powder/polymer composites with excellent shaping capability [7] and improved mechanical properties [8]. In addition, additive manufacturing has been recently employed to fabricate Ni-Mn-Ga complex shapes starting from powder samples [9–11]. Finally, by down-scaling, one can reach the properties of the material that do not necessarily appear when the material is in the bulk format [12–15]. Different pioneering works have been dedicated in down-scaling MSM Heuslers using several bottom-up and top-down approaches [16–18]. Specifically, starting from thin films of MSM Heuslers, the down-scaling approaches have been limited to nanosphere-lithography [15], photolithography [13,19,20], electron-beam lithography [6,21–26] and focused ion-beam milling techniques [27,28].

Searching for cost-effective down-scaling techniques starting from the continuous thin films, the solid-state dewetting process is known as an appropriate alternative. This process is a thermally activated top-down method based on the agglomeration of the material on the substrate, forming arrays of islands below the melting point of the material [29–31]. The driving force leading to such an effect is the free-energy minimization on the interfaces

between the film and the substrate at high-temperatures. The process initiates with the formation of holes, proceeds with the propagation and integration of the holes, and ends with the 3D islands of the material on the substrate [29,30]. Various parameters influence the size and density of the islands, among which are the initial thickness of the film, the temperature and time of heat treatment, the crystallography of the film, substrate, defects, the morphology of the film, etc. [30,32,33]. Dewetting processes have been so far reported for successfully down-scaling a number of single-element and binary alloys and compounds [33–40]. The first approach exploiting dewetting during deposition to induce arrays of holes in Ni-Mn-Ga-Co epitaxial films has been recently reported by Lünser et al. [41]. They took advantage of the initial stage of the dewetting process by growing thin films of various thicknesses (80–800 nm) at elevated temperatures (673–873 K). By adjusting the thickness and the growth temperature, they succeeded in controlling the size and distribution of the holes. Nevertheless, they have reported a significant composition variation of the material throughout the process, which inevitably influences the martensitic transformation and the magnetic properties of the films.

In this study, a different approach has been followed: performing post-deposition annealing at high-temperatures (1100–1150 K) in epitaxial Ni-Mn-Ga thin films grown on MgO(001) with thickness of 75 nm. The aim of the work is to complete the dewetting process by the formation of Ni-Mn-Ga islands. Morphology, composition, phase transformation and magnetic properties of the material have been investigated at each stage of the process.

2. Materials and Methods

Experimental

An epitaxial Ni-Mn-Ga film was deposited on MgO(001) substrate at elevated temperature. The epitaxial crystal relation is Ni-Mn-Ga(001)[100]/MgO(001)[110]. The growth condition and the composition of the film are summarized in Table 1.

Table 1. Pristine sample: thickness, deposition rate, deposition temperature, composition and Curie temperature.

Thickness (nm)	Dep. Rate (nm·s ⁻¹)	Temperature (K)	Composition (at. % ± 1)	T _C (K)
75	0.06	573	Ni _{50.0} Mn _{18.6} Ga _{31.4}	~344

The film was cut into several pieces of approximately “3 mm × 3 mm” for the annealing process. One piece was kept as a reference sample. To promote the dewetting process, the annealing treatment was performed in a furnace (Carbolite) by placing the sample in a quartz tube under a vacuum atmosphere (2×10^{-4} Pa) to avoid the oxidation of the film surface. The selected annealing temperatures (1100 to 1150 K) were reached using a heating rate of ~51 K/min. The samples were then kept at a fixed temperature for the entire annealing time (55 to 165 min). Six annealing conditions were performed as shown in Table 2.

Table 2. Sample annealing conditions and the measured composition of the samples after the heat treatment.

Sample	Annealing Temp. (K)	Annealing Time (min)	Composition (at. % ± 1)
1100_55	1100	55	Ni _{55.6} Mn _{21.0} Ga _{23.4}
1100_110	1100	110	Ni _{62.8} Mn _{13.3} Ga _{23.9}
1100_165	1100	165	Ni _{71.8} Mn _{15.1} Ga _{13.1}
1150_55	1150	55	Ni _{60.0} Mn _{20.4} Ga _{19.6}
1150_110	1150	110	Ni _{62.0} Mn _{22.3} Ga _{15.7}
1150_165	1150	165	Ni _{62.4} Mn _{14.3} Ga _{23.3}

Atomic and magnetic force microscopy (AFM/MFM) images were obtained using a Dimension 3100 scanning probe microscope equipped with a Nanoscope Veeco controller using MESP-V2 magnetic tips in the interleaved mode at room temperature. Backscattered electron (BSE) images, as well as material composition, were obtained by a scanning electron microscope (SEM) equipped with energy dispersive X-ray spectroscopy (EDS) and BSE detectors (SEM, FEI Inspect—F). Room-temperature magnetic hysteresis loops were measured using an alternating gradient force magnetometer (AGFM) by applying the magnetic field parallel to the film plane along MgO[100]. The magnetic signal of the sample holder was subtracted. The thermomagnetic curves were obtained using a superconducting quantum interference device (SQUID) magnetometer in the presence of a constant in-plane magnetic field along MgO[100] and the temperature ramp of $dT/dt = 0.5$ K/min.

3. Results and Discussion

Figure 1 summarizes the morphology and the magnetic characteristics of the pristine sample. The AFM images in Figure 1a demonstrate the presence of X-type twins that are characterized by different orientations of the twinning planes (i.e., at 45° degrees to the MgO(001) substrate) [42–47]. The corresponding out-of-plane contribution of the magnetic domains can be visualized in the MFM images as the dark and the bright contrasts (Figure 1b) [42–49]. When cooling from 400 K, the thermomagnetic curves of the pristine sample (Figure 1c) show an abrupt rise in the susceptibility at around 344 K, which is ascribed to crossing the austenitic Curie temperature of the sample [50], where it transforms from the paramagnetic austenitic phase to ferromagnetic austenitic phase. The susceptibility slightly drops afterwards by further cooling, due to martensitic transformation, where the sample transforms from the ferromagnetic austenitic phase to ferromagnetic martensitic phase. The drop of the signal is due to the lower magnetic susceptibility of the martensitic phase compared to the austenitic phase in the applied low magnetic field ($\mu_0 H = 2$ mT) [51]. Upon heating, the reverse transformation takes place, leaving the temperature hysteresis of the structural phase transformation. The pristine sample shows a broad martensitic transition that spans more than 100 K. It can be recognized by looking at the temperature hysteresis (the gap between the cooling and the heating curves). The cooling curve constitutes the upper branch of the gap because of the presence of residual high-susceptibility ferromagnetic austenitic phase in the transition state. Though at room temperature, the transformation is not complete according to the thermomagnetic curves, the magnetic hysteresis loops measured for the pristine sample at room temperature (Figure 1d) show the ferromagnetic characteristics of the material. The saturation magnetization, coercivity and remanent magnetization are $M_S = 48.4$ Am²/kg, $H_C = 10$ mT and $M_r = 6.2$ Am²/kg, respectively.

The morphology of the samples was evaluated by AFM after the annealing process (Figure 2). The images show the rough inhomogeneous surface of the samples. The roughness of the annealed samples shows an increase by a factor of up to around 30 with respect to the pristine sample.

The morphology of the annealed samples was evaluated in the larger scale by BSE imaging (Figure 3). This type of imaging directly provides information about the morphology of the samples; moreover, the contrast change can be attributed to the composition variation or/and the variation of the height with respect to the detector. By increasing the annealing time at 1100 K (Figure 3a–c), the holes propagate so that the sample annealed for 165 min shows the largest holes, largest total hole area, and the lowest number of holes (Table 3). However, the samples annealed at 1150 K show a considerable propagation of holes when increasing the annealing time to 110 min, where the holes are integrated constituting ~75% of the scan area (Figure 3g, Table 3). Therefore, the islands are completely isolated, showing the average size of ~ 0.49 μm^2 . In addition, the propagation of the islands and holes seems to follow a symmetric path. Specifically, this is more pronounced for samples 1100_110, 1100_165, and 1150_165. Large-scale BSE images of the samples 1100_110, 1100_165 are provided as examples. We calculated the approximate angles between the

symmetric paths that look like lines in large scales (Figure 3d,e). The direction of the lines can be categorized into a pair of orthogonal lines having relative in-plane misalignment of around 22° with respect to each other. Correspondingly, the lines are around 11° misaligned in the plane of the film with respect to the MgO[100] and MgO[010] directions (Figure 3d inset).

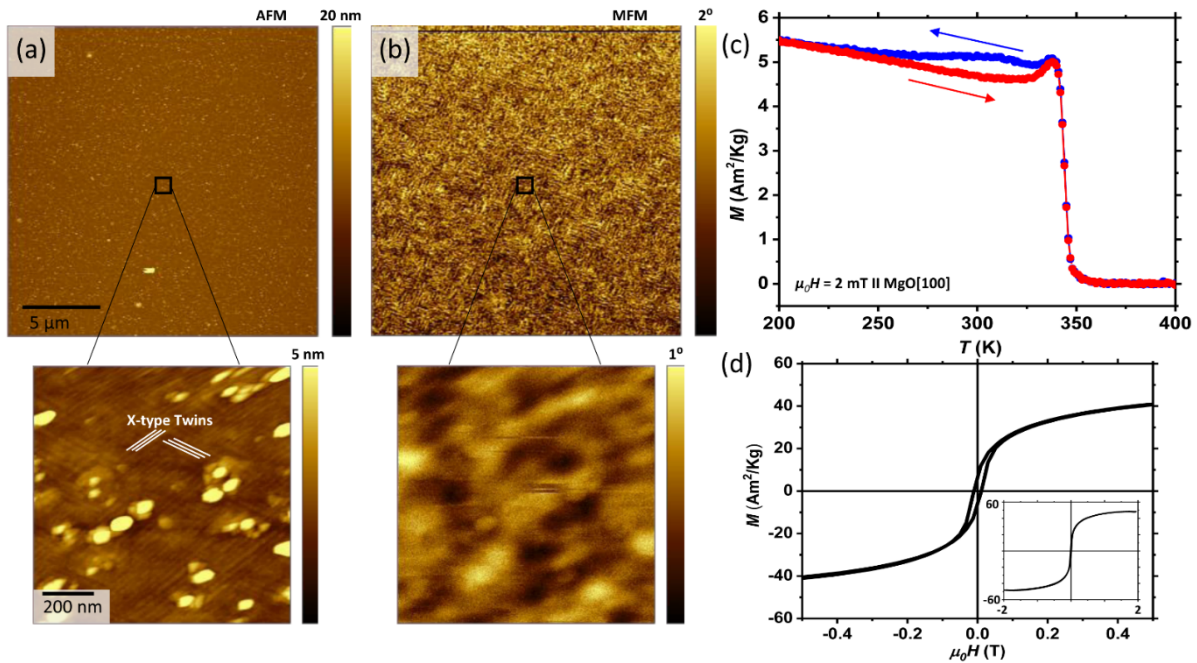


Figure 1. Pristine sample: (a) AFM at room temperature, (b) MFM at room temperature. (c) Thermomagnetic curves for the temperature range of 200–400 K applying low magnetic field ($\mu_0H = 2$ mT) in the plane of the film along MgO[100]. MgO[100] and MgO[010] directions are along the edges of the AFM/MFM images. (d) Magnetic hysteresis loops at room temperature applying external field along MgO[100] in the plane of the film. The inset shows the full graph.

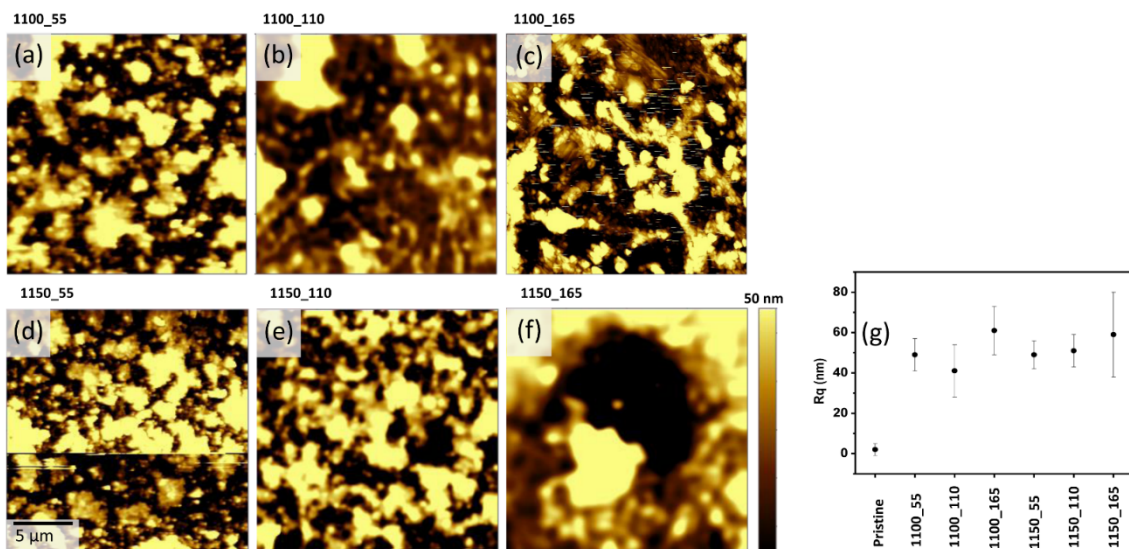


Figure 2. Annealed samples: AFM images of (a) 1100_55, (b) 1100_110, (c) 1100_165, (d) 1150_55, (e) 1150_110, (f) 1150_165. (g) Graph showing the roughness of the annealed samples with respect to the pristine sample. The height irregularities compared to the data variance is also provided as the data bars. MgO[100] and MgO[010] directions are along the edges of the AFM images.

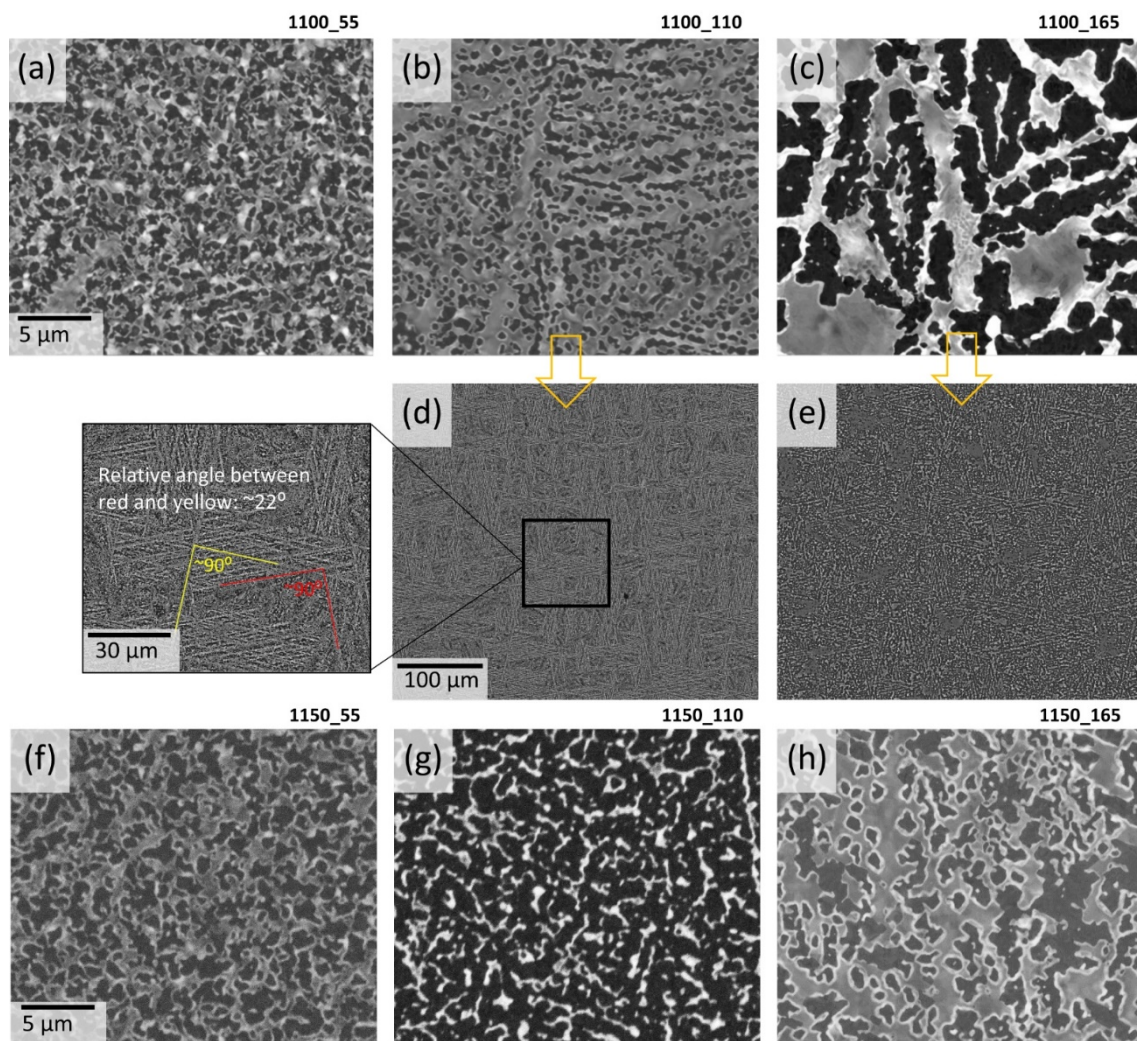


Figure 3. Annealed samples: BSE images of (a) 1100_55, (b) 1100_110, (c) 1100_165, (d) large-scale image of 1100_110, (e) large-scale image of 1100_165, (f) 1150_55, (g) 1150_110, (h) 1150_165. The inset in (d) is the magnified image of the marked area showing the relative orientation of the symmetric paths of islands with respect each other. MgO[100] and MgO[010] directions are along the edges of the BSE images.

Table 3. Morphology characteristics of the annealed samples estimated for Figure 3 (estimation uncertainty $\approx 10\%$). The average hole number and the average hole size are not applicable (NA) for 1150–110 sample because the holes are integrated (it is not possible anymore to count them as individual components).

Sample	Avg. Hole Number (μm^{-2})	Avg. Hole Size (μm^2)	Total Hole Area (%)
1100_55	1.2	0.33	40
1100_110	1.2	0.24	28
1100_165	0.1	6.26	50
1150_55	0.7	0.55	38
1150_110	NA	NA	75
1150_165	0.4	0.83	37

Room-temperature magnetic hysteresis loops of the samples were measured by applying an external magnetic field up to $\mu_0 H = |0.5|$ T in the plane of the films along MgO[100] (Figure 4). The M_{max} and M_r of the annealed samples show a significant reduction, but the

coercivity is in the same range of values compared to the pristine sample. The measured values are provided in Table 4. The hysteresis loops also show that annealing has changed the magnetic behavior of the samples. Annealed samples beside the ferromagnetic component show a paramagnetic component, which raises with the increase in the size of the islands in sample 1100–165.

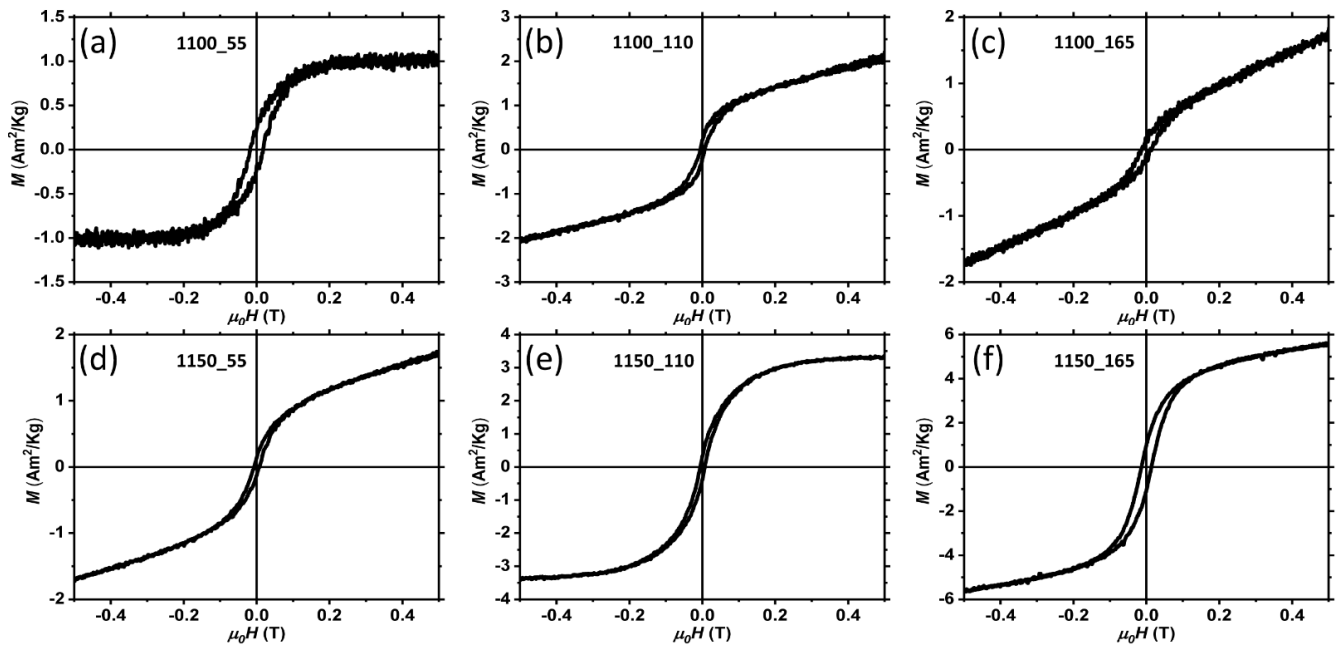


Figure 4. Magnetic hysteresis loops of the annealed samples at room temperature applying external field along MgO[100] in the plane of the films: (a) 1100_55, (b) 1100_110, (c) 1100_165, (d) 1150_55, (e) 1150_110, (f) 1150_165.

Table 4. Magnetic characteristics of the samples obtained from the magnetic hysteresis loops measured at room temperature.

Sample	M at 0.5 T (Am ² /kg)	M_r (Am ² /kg)	H_c (mT)
Pristine	40.8	~6.2	~10
1100_55	1.0	0.2	18
1100_110	2.0	0.2	6
1100_165	1.7	0.1	13
1150_55	1.7	0.1	7
1150_110	3.4	0.4	6
1150_165	5.6	1.0	14

Composition measurements gave us a deeper view of the evolution of the samples in the annealing process. Two different approaches have been taken:

1. Obtaining insight into the average percentage of the atomic contents of Ni, Mn and Ga at large-scale (Figure 5a,c, Table 2).
2. EDS mapping on small-scale to obtain information about the local distribution of the atoms in the annealed films (Figure 5b,d).

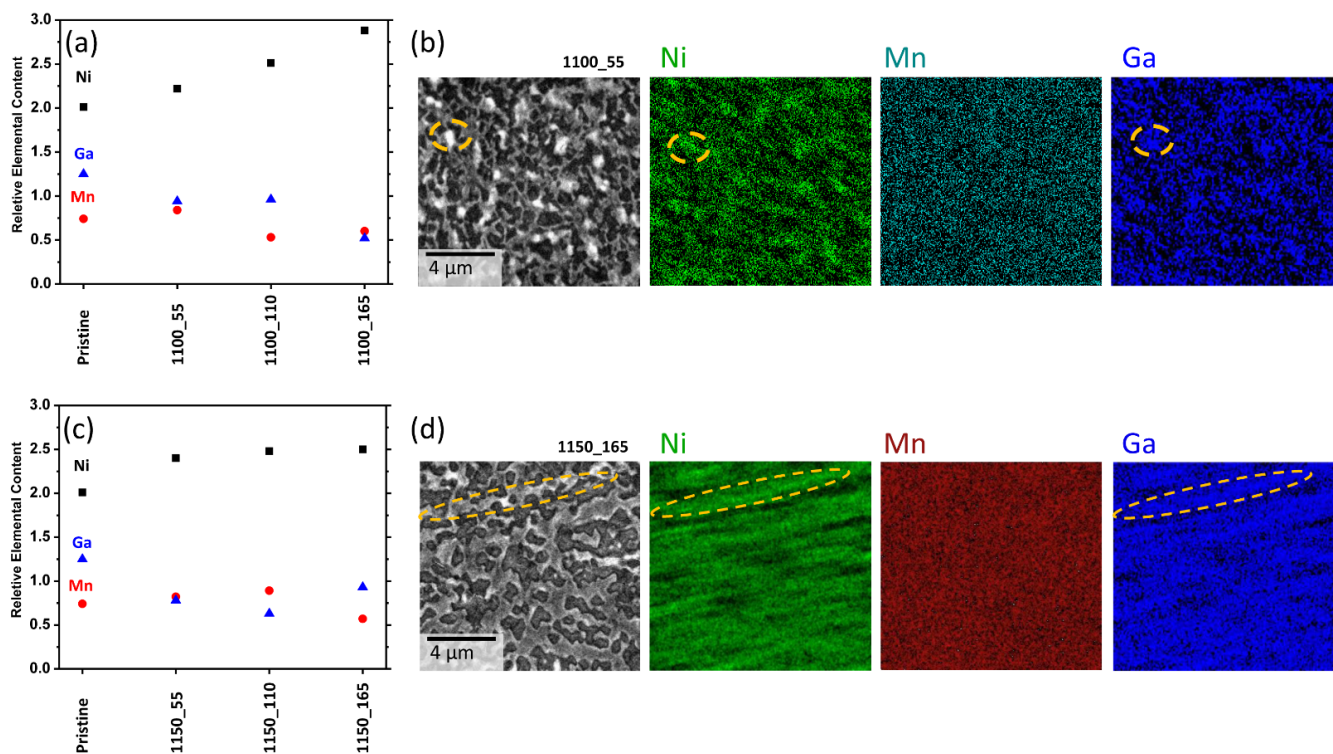


Figure 5. Composition measurements obtained by EDS: (a) the relative contents of each of the elements for the pristine and the annealed samples at 1100 K; (b) high-resolution elemental mapping of sample 1100_55 (c) the relative contents of each of the elements for the pristine and the annealed samples at 1150 K. (d) high-resolution elemental mapping of sample 1150_165. Some of the Ni- and Ga-rich areas are highlighted by yellow dash lines.

The first approach for the samples annealed at 1100 K (Figure 5a, Table 2) shows a continuous rise of Ni content at the expense of Ga and then Mn contents as a function of annealing time. This has pushed the composition of the annealed films far away from the stoichiometric Ni_2MnGa . Those results could be due to sublimation of Ga and then Mn at elevated temperatures and high vacuum. In addition to sublimation, our high-magnification composition mapping for 1100–55 sample shows small bright inclusions; one of these has been marked in Figure 5b. The inclusions show higher contents of Ni and Ga with respect to the matrix of the sample, revealing material elemental segregation in the annealing process. One could expect even more significant segregation by increasing the annealing time to 110 and 165 min. The samples annealed at 1150 K (Figure 5c, Table 2) also show a composition variation as a function annealing time. With respect to the samples annealed at 1100 K, the sublimation of Ga is more abrupt, whereas the Mn sublimation occurs only for the longest annealing time.

Thanks to the second approach of composition measurements (EDS mapping in small scale), we can confirm that the segregation process also exists in these samples. The high-magnification composition mapping of 1150_165 sample (Figure 5d) shows that the material islands' propagation lines are richer in Ni and Ga with respect to the matrix of the sample, whereas the Mn content is homogeneously distributed. The relatively homogenous distribution of the Mn content in the entire scan area (Figure 5b,d) also shows that the holes appearing in the SEM images do not pass through the entire film.

Finally, we measured the thermomagnetic curves of the samples to evaluate the susceptibility evolution as a function of temperature (Figure S1). Although the annealed samples are magnetic at room temperature, as shown in Figure 4, none of the samples underwent first/second order phase transformations in the investigated range of temperature (200–400 K). This could be due to severe composition variation and the phase segregation of the material in the annealing process. We believe that the magnetic signal of the annealed

samples at room temperature could possibly be due the presence of a secondary magnetic phase having T_c above 400 K.

In this work, we used the annealing temperature and time as the driving forces to control the dewetting process. Other parameters such as film thickness, type of gas, gas pressure, and substrate properties, which also contribute to determining the final morphology of the dewetted thin film, were kept constant. The selected temperatures and times successfully promoted the formation of holes and the propagation of holes. However, the magnetic and composition characterizations proved that these annealing parameters used to control the dewetting process are detrimental for these types of ternary compounds that have very sensitive composition-dependent transformations. The annealing parameters resulted in elemental sublimation, phase segregation, and, consequently, termination of first/second order phase transformation of the samples. The next direction of this interesting topic could be to promote the dewetting process at lower temperatures by regulating other parameters (e.g., type of gas, gas pressure, and type of substrate) in order to preserve the composition of the films and, consequently, preserve their peculiar magnetic properties through the dewetting process.

4. Conclusions

Dewetting process was studied in epitaxial Ni-Mn-Ga films deposited on MgO(001). The kinetics of the process have been followed by performing high-temperature annealing in the range of 1100–1150 K for increasing time (55 to 165 min). Scanning electron microscopy images revealed morphology evolution starting from the creation of holes in the continuous layer towards the formation of micro/nanoislands, occurring at increasing temperature and time. The annealing process progressively induced Ga and Mn sublimation accompanied by Ni-Ga segregation. Such a change has reflected into a progressive decrease of magnetic signal. The process completion leads to films containing islands that display a faint magnetic signal without any evidence of first/second order phase transformation.

Supplementary Materials: The following supporting information can be downloaded at: <https://www.mdpi.com/article/10.3390/cryst12121826/s1>, Figure S1: Thermomagnetic curves of the annealed samples for the temperature range of 200–400 K: (a) 1100_55, (b) 1150_55 applying low magnetic field ($\mu_0H = 2$ mT) in the plane of the film along MgO[100], (c) 1150_110, (d) 1150_165 applying magnetic field of ($\mu_0H = 150$ mT) in the plane of the film along MgO[100].

Author Contributions: Conceptualization, F.A.; investigation, M.T.G., F.C. (Federica Celegato) and G.B.; resources, M.T.G.; writing—original draft preparation, M.T.G.; writing—review and editing, G.B., F.C. (Francesca Casoli) and P.T.; visualization, M.T.G.; supervision, F.A. and P.T.; funding acquisition, F.A. and P.T. All authors have read and agreed to the published version of the manuscript.

Funding: This research received no external funding.

Data Availability Statement: Not applicable.

Acknowledgments: This work was partially supported by Fondazione Cariparma through the Biomontans project.

Conflicts of Interest: The authors declare no conflict of interest.

References

1. Jani, J.M.; Leary, M.; Subic, A.; Gibson, M.A. A review of shape memory alloy research, applications and opportunities. *Mater. Des.* **2014**, *56*, 1078–1113. [[CrossRef](#)]
2. Kohl, M.; Gueltig, M.; Pinneker, V.; Yin, R.; Wendler, F.; Krevet, B. Magnetic shape memory microactuators. *Micromachines* **2014**, *5*, 1135–1160. [[CrossRef](#)]
3. Rashidi, S.; Ehsani, M.H.; Shakouri, M.; Karimi, N. Potentials of magnetic shape memory alloys for energy harvesting. *J. Magn. Mater.* **2021**, *537*, 168112. [[CrossRef](#)]
4. Kitanovski, A. Energy applications of magnetocaloric materials. *Adv. Energy Mater.* **2020**, *10*, 1903741. [[CrossRef](#)]
5. Bruederlin, F.; Bumke, L.; Chluba, C.; Ossmer, H.; Quandt, E.; Kohl, M. Elastocaloric cooling on the miniature scale: A review on materials and device engineering. *Energy Technol.* **2018**, *6*, 1588–1604. [[CrossRef](#)]

6. Kohl, M.; Fechner, R.; Gueltig, M.; Megnin, C.; Ossmer, H. Miniaturization of Shape Memory Actuators. In Proceedings of the 16th International Conference on New Actuators, Bremen, Germany, 25–27 June 2018; pp. 1–9.
7. Rodríguez-Crespo, B.; Salazar, D.; Lanceros-Méndez, S.; Chernenko, V. Development and magnetocaloric properties of Ni (Co)-Mn-Sn printing ink. *J. Alloys Compd.* **2022**, *917*, 165521. [[CrossRef](#)]
8. Gao, P.; Tian, B.; Xu, J.; Tong, Y.; Chen, F.; Li, L. Investigation on porous NiMnGa alloy and its composite with epoxy resin. *J. Alloys Compd.* **2022**, *892*, 162248. [[CrossRef](#)]
9. Laitinen, V.; Saren, A.; Sozinov, A.; Ullakko, K. Giant 5.8% magnetic-field-induced strain in additive manufactured Ni-Mn-Ga magnetic shape memory alloy. *Scr. Mater.* **2022**, *208*, 114324. [[CrossRef](#)]
10. Ituarte, I.F.; Nilsén, F.; Nadimpalli, V.K.; Salmi, M.; Lehtonen, J.; Hannula, S.P. Towards the additive manufacturing of Ni-Mn-Ga complex devices with magnetic field induced strain. *Addit. Manuf.* **2022**, *49*, 102485. [[CrossRef](#)]
11. Caputo, M.P.; Berkowitz, A.E.; Armstrong, A.; Müllner, P.; Solomon, C.V. 4D printing of net shape parts made from Ni-Mn-Ga magnetic shape-memory alloys. *Addit. Manuf.* **2018**, *21*, 579–588. [[CrossRef](#)]
12. Bhattacharya, K.; DeSimone, A.; Hane, K.F.; James, R.D.; Palmstrøm, C.J. Tents and tunnels on martensitic films. *Mater. Sci. Eng. A* **1999**, *273–275*, 685–689. [[CrossRef](#)]
13. Dong, J.W.; Xie, J.Q.; Lu, J.; Adelmann, C.; Palmstrøm, C.J.; Cui, J.; Pan, Q.; Shield, T.W.; James, R.D.; McKernan, S. Shape memory and ferromagnetic shape memory effects in single-crystal Ni₂MnGa thin films. *J. Appl. Phys.* **2004**, *95*, 2593–2600. [[CrossRef](#)]
14. Thomas, M.; Heczko, O.; Buschbeck, J.; Lai, Y.W.; McCord, J.; Kaufmann, S.; Schultz, L.; Fähler, S. Stray-Field-Induced Actuation of Free-Standing Magnetic Shape-Memory Films. *Adv. Mater.* **2009**, *21*, 3708–3711. [[CrossRef](#)]
15. Campanini, M.; Nasi, L.; Fabbri, S.; Casoli, F.; Celegato, F.; Barrera, G.; Chiesi, V.; Bedogni, E.; Magén, C.; Grillo, V.; et al. Magnetic Shape Memory Turns to Nano: Microstructure Controlled Actuation of Free-Standing Nanodisks. *Small* **2018**, *14*, 1803027. [[CrossRef](#)]
16. Dunand, D.C.; Müllner, P. Size effects on magnetic actuation in Ni-Mn-Ga shape-memory alloys. *Adv. Mater.* **2011**, *23*, 216–232. [[CrossRef](#)]
17. Wang, C.; Meyer, J.; Teichert, N.; Auge, A.; Rausch, E.; Balke, B.; Hütten, A.; Fecher, G.H.; Felser, C. Heusler nanoparticles for spintronics and ferromagnetic shape memory alloys. *J. Vac. Sci. Technol. B* **2014**, *32*, 020802. [[CrossRef](#)]
18. Hennel, M.; Varga, M.; Frolova, L.; Nalevanko, S.; Ibarra-Gaytán, P.; Vidyasagar, R.; Sarkar, P.; Dzubinska, A.; Galdun, L.; Ryba, T.; et al. Heusler-Based Cylindrical Micro- and Nanowires. *Phys. Status Solidi A* **2022**, *219*, 2100657. [[CrossRef](#)]
19. Takhsha Ghahfarokhi, M.; Arregi, J.A.; Casoli, F.; Horký, M.; Cabassi, R.; Uhlíř, V.; Albertini, F. Microfabricated ferromagnetic-shape-memory Heuslers: The geometry and size effects. *Appl. Mater. Today* **2021**, *23*, 101058. [[CrossRef](#)]
20. Eichhorn, T.; Hausmanns, R.; Jakob, G. Microstructure of freestanding single-crystalline Ni₂MnGa thin films. *Acta Mater.* **2011**, *59*, 5067–5073. [[CrossRef](#)]
21. Lambrecht, F.; Lay, C.; Aseguinolaza, I.R.; Chernenko, V.; Kohl, M. NiMnGa/Si shape memory bimorph nanoactuation. *Shap. Mem. Superelasticity* **2016**, *2*, 347–359. [[CrossRef](#)]
22. Schmitt, M.; Backen, A.; Fähler, S.; Kohl, M. Development of ferromagnetic shape memory nanoactuators. In Proceedings of the 2012 12th IEEE International Conference on Nanotechnology (IEEE-NANO), Birmingham, UK, 20–23 August 2012; pp. 1–4.
23. Arivanandhan, G.; Li, Z.; Curtis, S.; Velvaluri, P.; Quandt, E.; Kohl, M. Temperature Homogenization of Co-Integrated Shape Memory—Silicon Bimorph Actuators. *Proceedings* **2020**, *64*, 8.
24. Kohl, M.; Schmitt, M.; Backen, A.; Schultz, L.; Krevet, B.; Fähler, S. Ni-Mn-Ga shape memory nanoactuation. *Appl. Phys. Lett.* **2014**, *104*, 043111. [[CrossRef](#)]
25. Lambrecht, F.; Sagardiluz, N.; Gueltig, M.; Aseguinolaza, I.R.; Chernenko, V.A.; Kohl, M. Martensitic transformation in NiMnGa/Si bimorph nanoactuators with ultra-low hysteresis. *Appl. Phys. Lett.* **2017**, *110*, 213104. [[CrossRef](#)]
26. Schmitt, M.; Backen, A.; Fähler, S.; Kohl, M. Freely movable ferromagnetic shape memory nanostructures for actuation. *Microelectron. Eng.* **2012**, *98*, 536–539. [[CrossRef](#)]
27. Jenkins, C.A.; Ramesh, R.; Huth, M.; Eichhorn, T.; Pörsch, P.; Elmers, H.J.; Jakob, G. Growth and magnetic control of twinning structure in thin films of Heusler shape memory compound Ni₂MnGa. *Appl. Phys. Lett.* **2008**, *93*, 234101. [[CrossRef](#)]
28. Mashirov, A.V.; Irzhak, A.V.; Tabachkova, N.Y.; Milovich, F.O.; Kamantsev, A.P.; Zhao, D.; Liu, J.; Kolesnikova, V.G.; Rodionova, V.V.; Koledov, V.V. Magnetostructural Phase Transition in Micro- and Nanosize Ni–Mn–Ga–Cu Alloys. *IEEE Magn. Lett.* **2019**, *10*, 1–4. [[CrossRef](#)]
29. Thompson, C.V. Solid-state Dewetting of Thin Films. *Annu. Rev. Mater. Res.* **2012**, *42*, 399–434. [[CrossRef](#)]
30. Leroy, F.; Borowik, Ł.; Cheynis, F.; Almadori, Y.; Curio, S.; Trautmann, M.; Barbé, J.C.; Müller, P. How to control solid state dewetting: A short review. *Surf. Sci. Rep.* **2016**, *71*, 391–409. [[CrossRef](#)]
31. Pierre-Louis, O. Solid-state wetting at the nanoscale. *Prog. Cryst. Growth Charact. Mater.* **2016**, *62*, 177–202. [[CrossRef](#)]
32. Motyčková, L. Magnetic Properties of Self-Assembled FeRh Nanomagnets. Master’s Thesis, Brno University of Technology, Brno, Czech Republic, 2020.
33. Barrera, G.; Celegato, F.; Cialone, M.; Coisson, M.; Rizzi, P.; Tiberto, P. Effect of the substrate crystallinity on morphological and magnetic properties of Fe₇₀Pd₃₀ nanoparticles obtained by the solid-state dewetting. *Sensors* **2021**, *21*, 7420. [[CrossRef](#)]
34. Andalouci, A.; Roussigné, Y.; Farhat, S.; Chérif, S.M. Magnetic and magneto-optical properties of assembly of nanodots obtained from solid-state dewetting of ultrathin cobalt layer. *J. Phys. Condens. Matter* **2019**, *31*, 495805. [[CrossRef](#)] [[PubMed](#)]

35. Barrera, G.; Celegato, F.; Coisson, M.; Cialone, M.; Rizzi, P.; Tiberto, P. Formation of free-standing magnetic particles by solid-state dewetting of Fe₈₀Pd₂₀ thin films. *J. Alloys Compd.* **2018**, *742*, 751–758. [[CrossRef](#)]
36. Oh, H.; Pyatenko, A.; Lee, M. A hybrid dewetting approach to generate highly sensitive plasmonic silver nanoparticles with a narrow size distribution. *Appl. Surf. Sci.* **2021**, *542*, 148613. [[CrossRef](#)]
37. Esterina, R.; Liu, X.M.; Adeyeye, A.O.; Ross, C.A.; Choi, W.K. Solid-state dewetting of magnetic binary multilayer thin films. *J. Appl. Phys.* **2015**, *118*, 144902. [[CrossRef](#)]
38. Bhalla, N.; Jain, A.; Lee, Y.; Shen, A.Q.; Lee, D. Dewetting metal nanofilms—Effect of substrate on refractive index sensitivity of nanoplasmonic gold. *Nanomaterials* **2019**, *9*, 1530. [[CrossRef](#)]
39. Song, X.; Liu, F.; Qiu, C.; Coy, E.; Liu, H.; Aperador, W.; Załęski, K.; Li, J.J.; Song, W.; Lu, Z.; et al. Nanosurfacing Ti alloy by weak alkalinity-activated solid-state dewetting (AAD) and its biointerfacial enhancement effect. *Mater. Horiz.* **2021**, *8*, 912–924. [[CrossRef](#)]
40. Motyčková, L.; Arregi, J.A.; Staňo, M.; Průša, S.; Částková, K.; Uhlíř, V. Preserving Metamagnetism in Self-Assembled FeRh Nanomagnets. *arXiv* **2022**, arXiv:2209.02469.
41. Lünser, K.; Diestel, A.; Nielsch, K.; Fähler, S. Self-Patterning of Multifunctional Heusler Membranes by Dewetting. *Adv. Mater. Interfaces* **2021**, *8*, 2100966. [[CrossRef](#)]
42. Diestel, A.; Neu, V.; Backen, A.; Schultz, L.; Fähler, S. Magnetic domain pattern in hierarchically twinned epitaxial Ni–Mn–Ga films. *J. Phys. Condens. Matter* **2013**, *25*, 266002. [[CrossRef](#)]
43. Ranzieri, P.; Fabbri, S.; Nasi, L.; Righi, L.; Casoli, F.; Chernenko, V.A.; Villa, E.; Albertini, F. Epitaxial Ni–Mn–Ga/MgO(100) thin films ranging in thickness from 10 to 100 nm. *Acta Mater.* **2013**, *61*, 263–272. [[CrossRef](#)]
44. Ranzieri, P.; Campanini, M.; Fabbri, S.; Nasi, L.; Casoli, F.; Cabassi, R.; Buffagni, E.; Grillo, V.; Magén, C.; Celegato, F.; et al. Achieving Giant Magnetically Induced Reorientation of Martensitic Variants in Magnetic Shape-Memory Ni–Mn–Ga Films by Microstructure Engineering. *Adv. Mater.* **2015**, *27*, 4760–4766. [[CrossRef](#)] [[PubMed](#)]
45. Niemann, R.; Backen, A.; Kauffmann-Weiss, S.; Behler, C.; Rößler, U.K.; Seiner, H.; Heczko, O.; Nielsch, K.; Schultz, L.; Fähler, S. Nucleation and growth of hierarchical martensite in epitaxial shape memory films. *Acta Mater.* **2017**, *132*, 327–334. [[CrossRef](#)]
46. Takhsha Ghahfarokhi, M.; Casoli, F.; Fabbri, S.; Nasi, L.; Celegato, F.; Cabassi, R.; Trevisi, G.; Bertoni, G.; Calestani, D.; Tiberto, P.; et al. Martensite-enabled magnetic flexibility: The effects of post-growth treatments in magnetic-shape-memory Heusler thin films. *Acta Mater.* **2020**, *187*, 135–145. [[CrossRef](#)]
47. Takhsha Ghahfarokhi, M.; Nasi, L.; Casoli, F.; Fabbri, S.; Trevisi, G.; Cabassi, R.; Albertini, F. Following the martensitic configuration footprints in the transition route of Ni–Mn–Ga magnetic shape memory films: Insight into the role of twin boundaries and interfaces. *Materials* **2020**, *13*, 2103. [[CrossRef](#)] [[PubMed](#)]
48. Takhsha Ghahfarokhi, M.; Chirkova, A.; Maccari, F.; Casoli, F.; Ener, S.; Skokov, K.P.; Cabassi, R.; Gutfleisch, O.; Albertini, F. Influence of martensitic configuration on hysteretic properties of Heusler films studied by advanced imaging in magnetic field and temperature. *Acta Mater.* **2021**, *221*, 117356. [[CrossRef](#)]
49. Casoli, F.; Varvaro, G.; Takhsha Ghahfarokhi, M.; Fabbri, S.; Albertini, F. Insight into the magnetisation process of martensitic Ni–Mn–Ga films: A micromagnetic and vector magnetometry study. *J. Phys. Mater.* **2020**, *3*, 045003. [[CrossRef](#)]
50. Albertini, F.; Solzi, M.; Paoluzi, A.; Righi, L. Magnetocaloric properties and magnetic anisotropy by tailoring phase transitions in NiMnGa alloys. *Mater. Sci. Forum* **2008**, *583*, 169–196. [[CrossRef](#)]
51. Kamarád, J.; Albertini, F.; Arnold, Z.; Casoli, F.; Pareti, L.; Paoluzi, A. Effect of hydrostatic pressure on magnetization of Ni_{2+x}Mn_{1-x}Ga alloys. *J. Magn. Magn. Mater.* **2005**, *290*, 669–672. [[CrossRef](#)]